UNIVERSIDAD NACIONAL DE COLOMBIA
SEDE MEDELLÍN
FACULTAD DE MINAS

DYNA
http://dyna.medellin.unal.edu.co/

Dual arm compressive spectral imaging in the visible and IR range

Yenni Paloma Villa-Acuña [a] & Henry Arguello-Fuentes [b]

[a] *Escuela de Ingenierías Eléctrica, Electrónica y de Telecomunicaciones, Universidad Industrial de Santander, Bucaramanga, Colombia. yenni.villa@correo.uis.edu.co*
[b] *Escuela de Ingeniería de Sistemas e Informática, Universidad Industrial de Santander, Bucaramanga, Colombia. henarfu@uis.edu.co*

Received: June 21th, 2015. Received in revised form: June 03rd, 2016. Accepted: July 21th, 2016.

Abstract
Imaging spectroscopy involves sensing spatial information in a scene across a range of wavelengths in order to acquire a three-dimensional data cube. Spectral images play an important role in science and technology. Some of their applications require image acquisition in both the visible and the infrared ranges in order to detect characteristics that are not noticeable to the bare eye. These can be perceived in lower layers of the scene where the visible radiation does not penetrate. This paper proposes a compressive image acquisition system that reduces the number of optical elements by jointly and compressively acquiring the images in the visible and infrared spectra. It also evaluates whether the quality of the reconstructed images is good enough to consider the optical implementation of the proposed system. Diverse simulations are performed to determine the peak signal to noise ratio (PSNR) of the data cubes as a function of the coded apertures transmittance, the Gaussian noise applied to the measurements and the number of snapshots. The simulations provide PSNR values of up to 33 dB in the reconstructed images.

Keywords: Spectral Imaging; Compressive Sensing; Dual arm; Infrared; Visible.

Sistema dual para muestreo compresivo de imágenes espectrales en el rango visible e infrarrojo

Resumen
La espectroscopia de imágenes involucra el muestreo de la información espacial de un objetivo a lo largo de un conjunto de longitudes de onda, en el que se adquiere un cubo de datos de tres dimensiones, dos de ellas espaciales y una espectral. Las imágenes espectrales juegan un papel importante en muchos campos de la ciencia y la tecnología, algunas de sus aplicaciones exigen la adquisición de la imagen en el espectro visible e infrarrojo, con el fin de detectar características no distinguibles a simple vista, presentes en capas inferiores del objetivo donde la luz visible no alcanza a atravesar. Este trabajo propone un sistema que reduce dichos costos de implementación adquiriendo simultáneamente y de forma comprimida la imagen en el espectro visible e infrarrojo. Además evalúa si la calidad de las imágenes reconstruidas es lo suficientemente buena para considerar su implementación óptica. Se realizaron diversas simulaciones para determinar la relación señal a ruido pico (PSNR, por su sigla en inglés) de los cubos de datos reconstruidos, en función de la transmitancia de los códigos de apertura, el ruido Gaussiano aplicado a las mediciones y el número de capturas. Los valores de PSNR obtenidos alcanzan los 33 dB.

Palabras clave: Imágenes Espectrales; Muestreo Compresivo; Sistema Dual; Infrarrojo; Visible.

1. Introduction

Spectrometers are instruments to measure the intensity or polarization of electromagnetic waves across a wide range of wavelengths, this is known as their spectral signature. Despite spectrometers providing precise spectral information for a specific spatial point, some applications are more interested in scanning the whole scene, thus involving all spatial points [1]. These instruments are known as spectral imagers as they acquire a scene's spatial (x, y) and spectral (λ) information in a 3D data cube. There are two main classes of spectral imagers, which can be either spectrally or spatially

How to cite: Villa-Acuña, Y. P. & Arguello-Fuentes, H. Dual arm compressive spectral imaging in the visible and IR range DYNA 83 (199) pp. 207-217, 2016

discriminatory. This depends on the dimension of the scan across the remaining 2D to complete the 3D data cube. An example of a spectrally discriminatory instrument is a 2D spatial camera based on bandpass filters [2]. This architecture is used to scan all spectral channels by sequentially tuning the bandwidth in steps. It requires the scene to be completely static during each spectral acquisition in order to acquire the same spatial matrix for every frequency range. The main drawback of this technique is that the number of zones to be scanned increases proportionally to the desired spatial or spectral resolution.

Conversely, in the relatively new compressive spectral imaging (CSI) approach, the detector measures 2D random coded compressed projections. In this, the number of required measurements for the reconstruction is far less than in the linear scanning case. CSI relies on CS principles: sparsity and incoherence [3,4].

The coded aperture snapshot spectral imager (CASSI) is an architecture that effectively applies the CS theory to improve the sensing speed and reduce the large amount of data to far fewer measurements than the ones established by the Nyquist/Shannon theorem. This makes it possible to acquire the entire data cube with just a few focal plane array (FPA) measurements [1-4]. The theoretical background of CASSI is applicable for any region of the electromagnetic spectrum determined by the spectral sensitivity of the optical elements. Therefore, as there is no technology developed in sensitive sensors that applies to such wide frequency ranges to capture images in both visible and infrared spectral bands, it is necessary to use an architecture that separately acquires the information through the appropriate detector. This could be created by using two CASSI systems separately, which results in an expensive system to implement. The dual arm (DA)-CASSI system is an alternative to reduce the implementation costs of the previous solution by jointly catching both ranges' spectral information. This system is proposed in this paper.

Spectral images play a very important role in various areas of science and technology such as: remote sensing [5], agriculture [6] and quality control [7]. Near infrared (NIR) spectroscopy utilizes the spectral information in the range from 780 to 2500 [ηm] to provide more complex structural information related to the combination of bonds' vibration. Numerous NIR studies demonstrate that the previous is a non-destructive and rapid technique -in the area of food quality assessment- since it reveals information related to the vibrational behavior of molecular bonds. Therefore, it can give details of the variety of molecules present in food [8]. For this reason, some applications require the image acquisition in both the visible (V) and infrared spectrum (IR) in order to detect characteristics not visible to the bare eye. These can be perceived in lower layers of the scene where the visible radiation does not penetrate [9]. Thus, not only visible but also infrared data is of the utmost interest for these applications. For this reason, the main objective of this paper is to design an optical architecture that allows multiple random projections of images to be acquired in the visible and infrared spectrum. It also includes the theoretical model and the evaluation of the reconstructed quality of the images in order to consider its optical implementation.

This paper is organized as follows: first, the background about CS theory and the multi-shot CASSI system are presented. There is also a brief explanation about system parallelization in order to separately acquire the image in each spectral range. After, the optical-mathematical model for the dual arm CASSI (DA-CASSI) system is presented. Finally, simulations and results to quantitatively compare the performance of the proposed system against two separate CASSI systems are presented.

2. Compressive sensing background

CS effectively reduces the acquisition time and the number of acquired measurements by simultaneously sensing and compressing the data instead of directly sensing the signal and then compressing it in the post processing stage. In this way, the cost of the system is reduced as well as its storage requirements. In order to do so, CS relies on two principles: sparsity and incoherence.

2.1. Sparsity

CS exploits the fact that many natural signals have a more compact representation on a convenient basis [3]. More formally, let $\mathbf{f} \in R^N$ be the signal of interest and, $\mathbf{f} = \mathbf{\Psi\theta}$ be the representation of $\mathbf{f}$ on the basis $\mathbf{\Psi}$. We can then say that $\mathbf{f}$ is $S - sparse$ if the orthonormal basis $\mathbf{\Psi} \in R^{NxN}$ sparsifies $\mathbf{f}$, when $\mathbf{\theta} = \mathbf{\Psi}^{\mathrm{T}}\mathbf{f}$ has only $S \ll N$ non-zero entries, where $\mathbf{\Psi}^{\mathrm{T}}$ is the transpose matrix of $\mathbf{\Psi}$. Otherwise, we can say that $\mathbf{\Psi}$ compresses $\mathbf{f}$, if the sorted by magnitude entries of θ decay according to $|\mathbf{\theta}(i)| < Ci^{-1/p}$ for any $p \leq 1$, and $C < \infty$. Then, it is said that $\mathbf{\theta}$ is S-compressible in $\mathbf{\Psi}$ by retaining the S largest coefficients by magnitude and setting the rest to zero [10].

A sparse representation means that the number of non-zero coefficients in $\mathbf{\theta}$ is S with $S \ll N$. A compressible representation, on the other hand, means that the coefficient's magnitudes on a given basis, when sorted, have fast power-law decay. Strictly speaking, most signals of interest are not exactly sparse but approximately sparse or compressible on a convenient basis, and the selection of the basis on which the signal is compressible is crucial in order to obtain better reconstruction results. Previous work has proven that the Kronecker product sparsifying basis gives the sparsest spectral images since such matrices act as sparsifying bases that jointly model the structure present in every signal dimension for multidimensional signals [10]. Suppose $\mathbf{F} \in \mathrm{R}^{\mathrm{MxNxL}}$ is a hyperspectral signal, or its vector representation $\mathbf{f} \in \mathrm{R}^{\mathrm{MNL}}$ is S-sparse on some basis $\mathbf{\Psi}_{3D}$, then $\mathbf{f}$ can be expressed as a linear combination of S vectors of $\mathbf{\Psi}_{3D}$ as follows:

$$\mathbf{f} = \mathbf{\Psi}_{3\mathrm{D}}\mathbf{\theta}, \tag{1}$$

where $S \ll MNL$ and $\mathbf{\Psi}_{3D}$ is the Kronecker product of three basis $\mathbf{\Psi}_1 \otimes \mathbf{\Psi}_2 \otimes \mathbf{\Psi}_3$. Usually, $\mathbf{\Psi}_{3D}$ is set to be the Kronecker product of the 2D-Wavelet symmlet 8 basis (used for the spatial dimensions) and the 1D-DCT basis (for the spectral), such that $\mathbf{\Psi}_{3\mathrm{D}} = \mathbf{\Psi}_{\mathrm{W2D}} \otimes \mathbf{\Psi}_{\mathrm{DCT}}$ [11,12].

2.2. Incoherence

The compressibility of spectral images also depends on how similar the sparsifying and the sensing basis are, which can be quantified by their mutual coherence. Mathematically, the mutual coherence of two orthonormal bases $\mathbf{\Phi} \in \mathbb{R}^{N\times N}$ and $\mathbf{\Psi} \in \mathbb{R}^{N\times N}$ is defined as the maximum absolute value for the inner product between elements of two bases, as follows:

$$\mu(\mathbf{\Phi}, \mathbf{\Psi}) = \sqrt{N} \cdot \max_{1\leq k,j\leq N} |< \mathbf{\Phi}_k, \mathbf{\Psi}_j >|. \quad (2)$$

In this case, $\mathbf{\Psi}$ and $\mathbf{\Phi}$ are the sparsifying and sensing bases, respectively, $\mathbf{\Psi}_j(t)$ is the j^{th} column of the representation basis matrix and, $\mathbf{\Phi}_k(t)$ is the k^{th} row of the sensing matrix. From eq. (2), if $\mathbf{\Psi}$ and $\mathbf{\Phi}$ contain correlated elements, the coherence is large. Otherwise, it is small. Thus, a lower value of μ indicates lower coherence or better incoherence between the measurement and the sparsifying basis. For CS, smaller mutual coherence values demand fewer measurements to achieve a certain accuracy in the reconstructed signals. For this reason, as random matrices are largely incoherent with any fixed basis $\mathbf{\Psi}$, the selection of an orthobasis $\mathbf{\Phi}$ uniformly at random promotes CS efficiency [3].

2.3. CASSI background

The CASSI system depicted in Fig. 1 is composed by six optical elements: an objective lens that focuses scene $\mathbf{F}$ onto the fixed coded aperture (CA); a set of coded apertures $\mathbf{T}^{\ell}$ to perform the coding, with $\ell = \{1, \dots, K\}$ and K the total number of shots; a band pass filter that limits the incoming source; a dispersive element S_k to shift the coded field horizontally; and an imaging lens to relay the coded filtered and spectrally sheared field onto the FPA image plane where it is finally integrated over the spectral sensitivity $\Delta\Lambda$.

Assuming that all optical elements are ideal, including linear dispersion by the dispersive element, the ℓ^{th} FPA measurement in the (m, n) pixel, $G^{\ell}_{m,n}$, can be expressed as:

$$G^{\ell}_{m,n} = \sum_{k=0}^{L-1} F_{m,n-k,k}\, T^{\ell}_{m,n-k} + \omega_{m,n}\,, \quad (3)$$

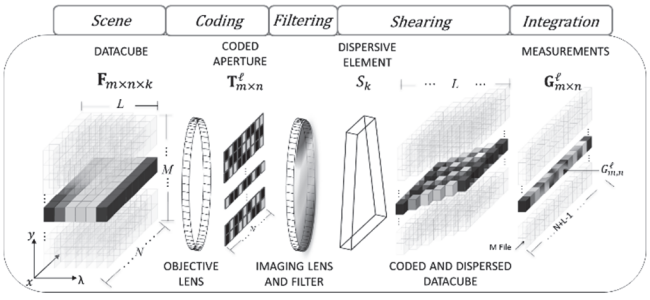

Figure 1. Light propagation through the CASSI system. The input signal $\mathbf{F}$ is coded by the CA $\mathbf{T}^{\ell}$, filtered and then dispersed by the prism $\boldsymbol{S_K}$. Finally, the coded and dispersed signal is integrated on the FPA detector.
Source: Adapted from [12].

where L is the total number of resolvable bands and ω is the noise present in the system. Let $\mathbf{g}^{\ell}$ denote the vector representation of the ℓ^{th} FPA measurements $\mathbf{G}^{\ell}$, which is written in matrix form as $\mathbf{g}^{\ell} = \mathbf{H}^{\ell}\mathbf{f}$, where $\mathbf{H}^{\ell}$ is the transfer function that accounts for the effects of the dispersive element and the ℓ^{th} CA. The set of K FPA measurements can then be assembled as $\mathbf{g} = [(\mathbf{g}^0)^{\mathrm{T}}, \dots, (\mathbf{g}^{\ell})^{\mathrm{T}}, \dots, (\mathbf{g}^{K-1})^{\mathrm{T}}]^{\mathrm{T}}$, which, in turn, can be expressed as:

$$\mathbf{g} = \mathbf{H}\mathbf{f} + \boldsymbol{\omega}, \quad (4)$$

where $\mathbf{H} = [(\mathbf{H}^0)^{\mathrm{T}}, \dots, (\mathbf{H}^{\ell})^{\mathrm{T}}, \dots (\mathbf{H}^{K-1})^{\mathrm{T}}]^{\mathrm{T}}$ is the vertical concatenation of the $\mathbf{H}^{\ell}$ matrices.

The CASSI principles that are described above are general and applicable to imaging in any region of the electromagnetic spectrum that is determined by the spectral sensitivity of all the optical elements. To acquire It is possible to create a scene's spectral information in both visible and IR range by using two CASSI systems separately so that each one acquires the image in a different spectral range. However, in order to reduce implementation costs, an architecture that jointly senses the scene in both ranges and also gives the information separated on the correspondent detector is proposed in the following section.

3. Dual-Arm (DA)-CASSI system.

Fig. 2 depicts the DA-CASSI architecture. It is composed of two arms corresponding to the visible and IR paths. When the impinging light source focused by the objective is coded by the DMD, the coded field is divided and addressed by the beam splitter towards each path. Both arms are composed by a band pass filter that band limits the incoming fields; a dispersive element (usually a prism), which horizontally shears the filtered and coded fields; and the appropriate FPA detector, into which the resulting spectral densities are finally integrated.

3.1. DA-CASSI mathematical model

The light propagation in the optical system begins when the reflected light source is focused by the objective lens into the CA, where the coding is realized by applying $T(x, y)$ to the spatio-spectral density source $f_o(x, y, \lambda)$. This yields $f_1(x, y, \lambda)$

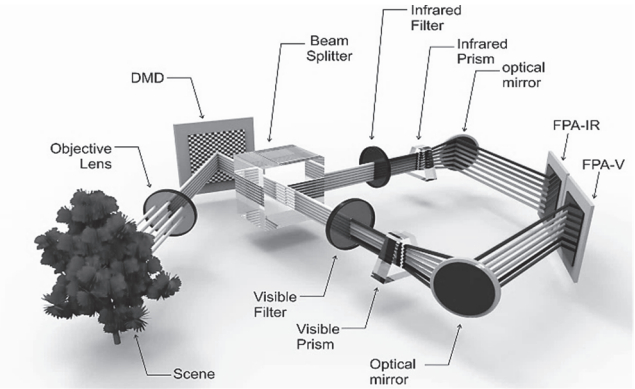

Figure 2. DA-CASSI optical architecture.
Source: The authors.

$$f_1(x,y,\lambda) = T(x,y) f_o(x,y,\lambda), \tag{5}$$

where (x,y) are the spatial coordinates and λ is the wavelength of the impinging light. The spectral density $f_1(x,y,\lambda)$ power is equally divided by the beam splitter and sent to the respective arm's filter. In each path, only the wavelengths belonging to that spectral range will pass to the corresponding prism where they will consequently be dispersed. This will result in the following coded fields:

$$\begin{aligned} f_{2\mathrm{V}}(x,y,\lambda) &= \iint f_{1\mathrm{V}}(x,y,\lambda) h_{\mathrm{V}}(x' - x \\ &\quad - S_{\mathrm{V}}(\lambda), y' - y) dx' dy', \\ f_{2\mathrm{IR}}(x,y,\lambda) &= \iint f_{1\mathrm{IR}}(x,y,\lambda) h_{\mathrm{IR}}(x' - x \\ &\quad - S_{\mathrm{IR}}(\lambda), y' - y) dx' dy', \end{aligned} \tag{6}$$

where h_V and h_{IR} are the optical impulse responses of the system for the visible and infrared systems, respectively, $S_V(\lambda)$ and $S_{IR}(\lambda)$ are the dispersion functions induced by the prisms and corresponding to each spectral range. Finally, $f_{1V}(x,y,\lambda)$ and $f_{1IR}(x,y,\lambda)$ are the filtered versions of $f_1(x,y,\lambda)$ in the visible and IR respectively.

Every coded and dispersed field is focused by an imaging lens into the respective FPA where they are integrated over the detector's spectral range sensitivity.

$$\begin{aligned} g_{\mathrm{V}}(x,y) &= \int_{\lambda_o}^{\lambda_{\mathrm{V}}} f_{2\mathrm{V}}(x,y,\lambda) d\lambda, \\ g_{\mathrm{IR}}(x,y) &= \int_{\lambda_{\mathrm{V}}}^{\lambda_{\mathrm{IR}}} f_{2\mathrm{IR}}(x,y,\lambda) d\lambda \end{aligned} \tag{7}$$

where the primed variables refer to the spatial location before the CA and the non-primed in the FPA.

Assuming that (i), the PSF h_V and h_{IR} are shift invariant; (ii) there is a one-to-one match between coded aperture features and the detectors' pixels and; (iii) supposing idealities in the optical elements, including linear dispersion by the dispersive element, the measurements at the detectors can be expressed as:

$$\begin{aligned} g_{\mathrm{V}}(x,y) &= \int_{\lambda_o}^{\lambda_{\mathrm{V}}} f_o(x - S_{\mathrm{V}}(\lambda), y, \lambda) T(x \\ &\quad - S_{\mathrm{V}}(\lambda), y) d\lambda, \\ g_{\mathrm{IR}}(x,y) &= \int_{\lambda_{\mathrm{V}}}^{\lambda_{\mathrm{IR}}} f_o(x - S_{\mathrm{IR}}(\lambda), y, \lambda) T(x \\ &\quad - S_{\mathrm{IR}}(\lambda), y) d\lambda. \end{aligned} \tag{8}$$

For analysis and computational purposes, the underlying analog phenomenon is discretized such that the spatio-spectral signal $f_o(x,y,\lambda)$ is defined as $\mathbf{F}_{m,n,k}$, and its vector representation is assembled as $\mathbf{f} = [\mathbf{f}_{\mathrm{V}}; \mathbf{f}_{\mathrm{IR}}]$, where (n,m) indexes the spatial axes (x,y) and k the spectral axis λ. The discretized coded aperture is represented by $\mathbf{T}$. Assuming that the visible filter limits the spectral components between $\{\lambda_0 - \lambda_{\mathrm{V}}\}$ and the infrared between $\{\lambda_{\mathrm{V}} - \lambda_{\mathrm{IR}}\}$, the total number of resolvable bands L is limited by $L_{\mathrm{V}} = \frac{\lambda_{\mathrm{V}} - \lambda_{\mathrm{o}}}{N_{\mathrm{V}}}$ and $L_{\mathrm{IR}} = \frac{\lambda_{\mathrm{IR}} - \lambda_{\mathrm{V}}}{N_{\mathrm{IR}}}$, where the spectral resolution is given by N_{V} and N_{IR}. Fig. 3 depicts the discretized model of the light propagation through the DA-CASSI system.

According to Fig. 3, the discretized output in each detector is modeled as the independent sum of the underlying spectral voxel slices that are modulated by the same coded aperture **T** and dispersed by the corresponding prism.

More strictly, the two FPA measurements in m,n for each detector can be expressed as:

$$\begin{aligned} (G_V)_{m,n} &= \sum_{k=0}^{L_V - 1} (F_V)_{m,n-k,k} \, T_{m,n-k} \\ &\quad + (\omega)_{m,n}, \\ (G_{IR})_{m,n} &= \sum_{k=L_V}^{L_{IR} - 1} (F_{IR})_{m,n-k,k} \, T_{m,n-k} \\ &\quad + (\omega)_{m,n}. \end{aligned} \tag{9}$$

In matrix form, eq. (9) can be expressed as eq. (4); however, the structure of the sensing matrix is represented as a diagonal matrix where the first sub matrix corresponds to the visible spectrum $\mathrm{H_V}$ and the second to the infrared $\mathrm{H_{IR}}$, as follows:

$$\underbrace{\begin{bmatrix} \mathbf{g}_{\mathrm{V}} \\ \mathbf{g}_{\mathrm{IR}} \end{bmatrix}}_{\mathbf{g}} = \overbrace{\begin{bmatrix} \mathbf{H}_{\mathrm{V}} & \mathbf{0} \\ \mathbf{0} & \mathbf{H}_{\mathrm{IR}} \end{bmatrix}}^{\mathbf{H}} \underbrace{\begin{bmatrix} \mathbf{f}_{\mathrm{V}} \\ \mathbf{f}_{\mathrm{IR}} \end{bmatrix}}_{\mathbf{f}} + \boldsymbol{\omega} \tag{10}$$

An example of the sensing matrix **H** is illustrated in Fig. 4. This matrix has a diagonal pattern where the circled diagonal vectors repeating horizontally correspond to the distribution of the coded aperture used for both the visible (top left) and infrared (bottom right) ranges.

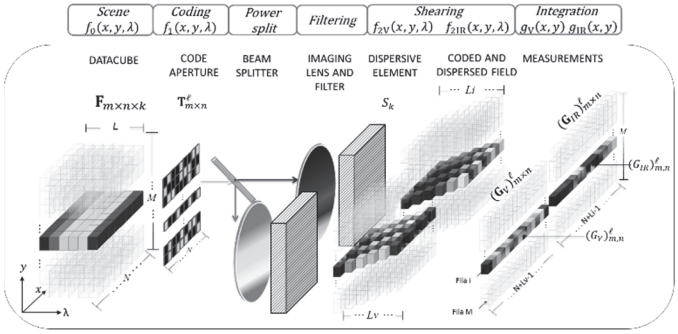

Figure 3. Light propagation through the DA-CASSI. The input signal **F** is coded by the CA, $\mathbf{T}^{\ell}$; the resulting field power is equally divided by the beam splitter and sent to both arms, where it will be filtered and then dispersed by the prism S_k. Finally, each coded and dispersed field is integrated into the respective detector.
Source: The authors.

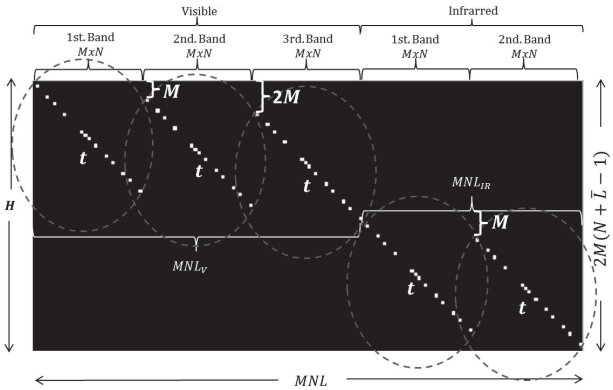

Figure 4. Single shot sensing matrix H example for $\boldsymbol{M = 4}$, $\boldsymbol{N = 8}$, $\boldsymbol{L_V = 3}$ and $\boldsymbol{L_{IR} = 2}$. Black squares represent zero-valued elements (blocking light) and the white squares represent one value elements. Notice that the coded aperture $\boldsymbol{t}$, is the same for the visible and infrared range.
Source: The authors.

In order to increase the number of compressive measurements when spectrally rich or very detailed spatial scenes are sensed, the multi-shot DA-CASSI allows multiple FPA measurements [11] to be acquired, each using a different CA during the integration time of the detector. This can be accomplished in two different ways: a) by moving a printed thin-film-based CA [13] back and forth using a high precision piezo-electric device to accurately perform the nanoposition realignment procedure (which significantly increases the system costs), or b) by using a DMD-based CA [14] that takes advantage of its tilting capabilities to address or deflect the impinging source light to the objective without requiring realignment. Therefore, the DMD-based CA becomes the best practical implementation since it offers a more robust, accurate and reliable multi-shot modulation system at a reduced cost [12].

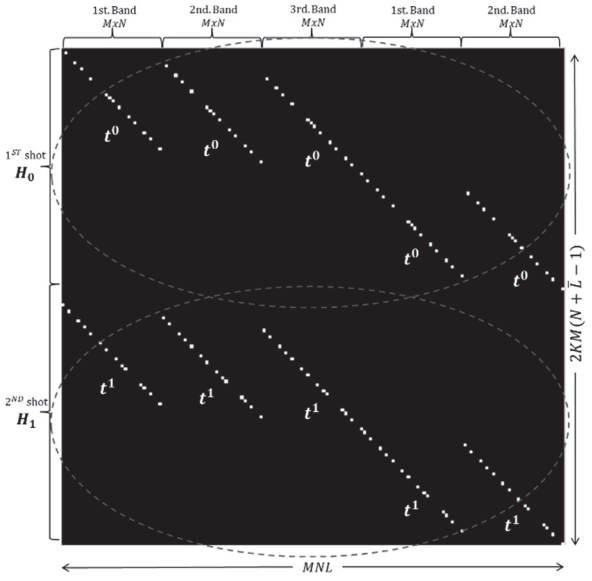

Figure 5. Multi-shot H matrix example for $\boldsymbol{K = 2, M = 4, N = 8, L_V = 3}$ and $\boldsymbol{L_{IR} = 2}$. Each circle pattern corresponds to every snapshot taken. Notice that $\mathbf{t^0}$ and $\mathbf{t^1}$ are the vector representations of the code apertures $\mathbf{T^0}$ and $\mathbf{T^1}$ respectively.
Source: The authors.

The $\mathbf{H}$ matrix for the multi-shot DA-CASSI system can also be expressed as in the conventional CASSI, eq. (4), since the modification is implicit for every $\mathbf{H}^{\ell} = [\,{\mathbf{H_V}}^{\ell}\ \mathbf{0}; \mathbf{0}\ {\mathbf{H_{IR}}}^{\ell}]$. Fig. 5 shows an example of a multi-shot $\mathbf{H} = [(\mathbf{H}^0)^{\mathrm{T}} \ldots (\mathbf{H}^{\ell})^{\mathrm{T}^{\ell}} \ldots (\mathbf{H}^{\mathrm{K}})^{\mathrm{T}}]$ matrix for *M=4, N=8, K=2* and *L=5*. In this matrix, three bands for the visible and two for the infrared range are used. The upper half of this matrix corresponds to the first shot and the lower half matrix accounts for the second.

Finally, the multi-shot vector of measurements is given by the following expression:

$$\begin{bmatrix} \mathbf{g}^0 \\ \vdots \\ \mathbf{g}^{\ell} \\ \vdots \\ \mathbf{g}^{\mathrm{K}-1} \end{bmatrix} = \begin{bmatrix} \mathbf{H}^0 \\ \vdots \\ \mathbf{H}^{\ell} \\ \vdots \\ \mathbf{H}^{\mathrm{K}-1} \end{bmatrix} \mathbf{f} + \boldsymbol{\omega}. \tag{11}$$

It can be noticed that the $\mathbf{H}$ matrix in eq. (11) is sparse and highly structured. Each row contains at most $L_{\mathrm{V}} + L_{\mathrm{IR}}$ non-zero elements, and each column contains up to K non-zero elements.

The non-linear dispersion curve of the prisms and other elements such as the imaging or objective lenses, the spectral response of the camera and the coded apertures might be considered ideal mathematically as long as a prior calibration process is conducted in order to partially mitigate all the deviations from the ideal characteristics assumed.

As shown in Fig. 2, the source light splits after the modulation undertaken by the DMD. For this reason, the DA-CASSI does not require an objective lens and a DMD as two CASSI systems are used simultaneously in parallel for the same purpose. This significantly reduces the total costs of the proposed system. Notice that the $\mathbf{f}_{\mathrm{V}}$ and $\mathbf{f}_{\mathrm{IR}}$ images are implicitly aligned in the DA-CASSI, whereas the separate CASSI systems need to be aligned to acquire the same spatial matrix.

3.2. DA-CASSI Reconstruction Process

As the number of voxels (columns of $\mathbf{H}$) is greater than the number of detector pixels (rows of $\mathbf{H}$) obtained, the system of linear equations represented by $\mathbf{H}$ becomes under-determined or ill-conditioned, hence direct inversion of the transfer function $\mathbf{H^{-1}}$ is unfeasible. However, several numerical algorithms have been designed to solve these kinds of convex unconstrained optimization problems. The gradient projection for the sparse reconstruction (GPSR) is one such example, and it is employed to obtain an approximation $\hat{\mathbf{f}}$ of the original data cube $\mathbf{f}$. This provides a good trade-off between computational complexity and reconstruction quality. The complexity per GPSR iteration is better explained in [15].

The set of measurements acquired by the FPA $\mathbf{g}$ is used as an input to the GPSR algorithm, and the reconstruction is attained by solving the optimization problem:

$$\hat{\mathbf{f}} = \boldsymbol{\Psi}^{\mathrm{T}} \left(\underset{\boldsymbol{\theta}}{\operatorname{argmin}} \|\mathbf{H}\boldsymbol{\Psi}\boldsymbol{\theta} - \mathbf{g}\|_2^2 + \tau\|\boldsymbol{\theta}\|_1 \right), \quad (12)$$

where τ is a regularization constant, $\mathbf{H}$ is the sensing matrix in eq. (10), $\boldsymbol{\theta}$ is a sparse representation of $\mathbf{f}$ on basis $\boldsymbol{\Psi}$ and the ℓ_1 minimization norm turns small components of $\boldsymbol{\theta}$ to zero and helps to boost sparse solutions. As the GPSR finds a sparse representation of the original data cube in the given basis $\boldsymbol{\Psi}$, to obtain $\hat{\mathbf{f}}$ from the coefficients given by the GPSR, they must be returned to their original domain by applying $\boldsymbol{\Psi}^{\mathrm{T}}$.

Notice that the DA-CASSI reconstruction process uses $2KM(N + \bar{L} - 1)$ measurements per iteration to recover $\mathbf{f}$, compared with the parallelized CASSI systems where only $KM(N + L_V - 1)$ or $KM(N + L_{IR} - 1)$ measurements are employed to separately obtain $\mathbf{f}_{\mathrm{V}}$ and $\mathbf{f}_{\mathrm{IR}}$ respectively.

4. Coded apertures design, compression ratio and Gaussian noise

The design of the coded aperture used to modulate the source light plays an important role in the reconstructed signal quality since this sets up the spatial modulation. Traditionally, the coded apertures employed in the CASSI system include Boolean [11,13], Bernoulli [12] and gray scaled [16] codes designed randomly [11-13], or they follow a Hadamard structure [11,16]. However, a recent work developed in order to enrich coding strategies proposed the use of colored coded apertures. This would replace the block-unblock photomasks with patterned optical filter arrays as a combination of low-pass, high-pass and band-pass filters so that every pixel from the coded aperture only allows a desired set of wavelengths to pass. This permits the modulation of the scene, not only spatially but also spectrally [12]. When developing this work, we used Boolean random coded apertures in order to employ every pixel of the coded aperture, $T^{\ell}_{\mathrm{m,n}} \in \{0,1\}$, with $T^{\ell}_{m,n} = 1$ representing a transmissive code element and $T^{\ell}_{m,n} = 0$ a blocking code element. The transmittance ξ of the coded aperture is defined as:

$$\xi = \sum_{m=0}^{M-1} \sum_{n=0}^{N-1} \frac{T_{m,n}}{MN}, \quad (13)$$

where MN represents the size of the coded aperture. Fig. 6 represents the transmittance concept. The pattern in Fig. 6a is blocking a greater number of pixels (a smaller transmittance) than that in Fig. 6c.

In addition to the transmittance, another important variable to analyze is the number of captured snapshots K [4, 11-14]. The compression ratio is the relation between the number of measurements acquired and the size of the spectral image to recover. As such, the compression ratio ρ can be expressed as a linear function of the number of shots K in the following way:

$$\rho = \frac{K\left(2M\left(N + \bar{L} - 1\right)\right)}{(MNL)}, \quad (14)$$

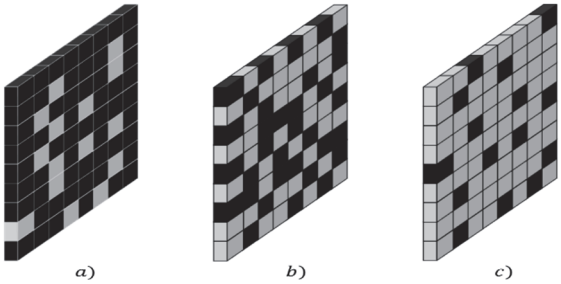

Figure 6. Coded apertures of 9x8 pixels with a transmittance of a) 20%. b) 50%. c) 80%. The block squares represent blocking elements whilst white squares permit the light to go through.
Source: The authors.

where $\bar{L}$ is the average between the number of visible and infrared bands.

In any real application, the measurements acquired are corrupted by at least a small amount of noise as sensing devices do not have infinite precision. In order to analyze the impact caused by different amounts of sensor noise, zero-mean Gaussian noise $\boldsymbol{\omega}$ was added to the set of FPA measurements $\mathbf{g}$, as in eq. (11). The variance of the noise is selected so we achieved a desired signal to noise ratio (SNR). The SNR can be expressed as:

$$\mathrm{SNR} = 10 \log_{10}\left(\frac{\sigma_g^2}{\sigma_n^2}\right), \quad (15)$$

where σ_g^2 is the variance of the FPA measurement set $\mathbf{g}$, and σ_n^2 is the variance of the noise.

5. Computer simulations and results

Diverse simulations were performed using two hyperspectral data cubes that were acquired with the AVIRIS sensor [17]. The selected scenes were found in AVIRIS' official website: Moffet and Salinas fields. Both hyperspectral images were acquired between 400 to 2500 [ηm], and contained 224 spectral reflectance bands. For each of the scenes' bands, the data was rescaled so that only 128x128 pixels are used due to the restriction of using only dyadic numbers that were required for the fast implementation of the 2-D wavelet transform. Furthermore, once the water absorption bands were removed, the remaining bands were linearly averaged so that the final data had 8 bands for the visible range and 8 bands for the IR.

For the first data set, the Moffet field aerial view, contains 16 classes of agricultural components such as corn, oats, wheat, woods, grass, etc. The original spatial resolution is 1924x753 pixels. The number of bands was reduced to 190 by removing bands covering the water absorption region: {1328.125 ηm – 1440.625 ηm}, {1487.500 ηm – 1515.625 ηm} and {1834.375 ηm – 1984.375 ηm}. An RGB representation of this database is presented in the upper left of Fig. 7. Here, the eight visible spectral bands are represented with their corresponding wavelength by using false color, and the remaining eight bands belonging to the

IR spectrum on gray scale.

The second spectral image was acquired over "Salinas Valley", California. The original image size in pixels is 512x217, and, as in the "Moffet Field" data cube, 36 water absorption bands were discarded from the 224 original ones. However, in this case, the removed bands were: {400.000 ηm – 428.125 ηm}, {1393.750 ηm – 1478.125 ηm}, {1815.625 ηm – 1975 ηm} and {2462.500 ηm – 2490.625 ηm}. This scene includes vegetables, bare soils, and vineyard fields, as shown in Fig. 8.

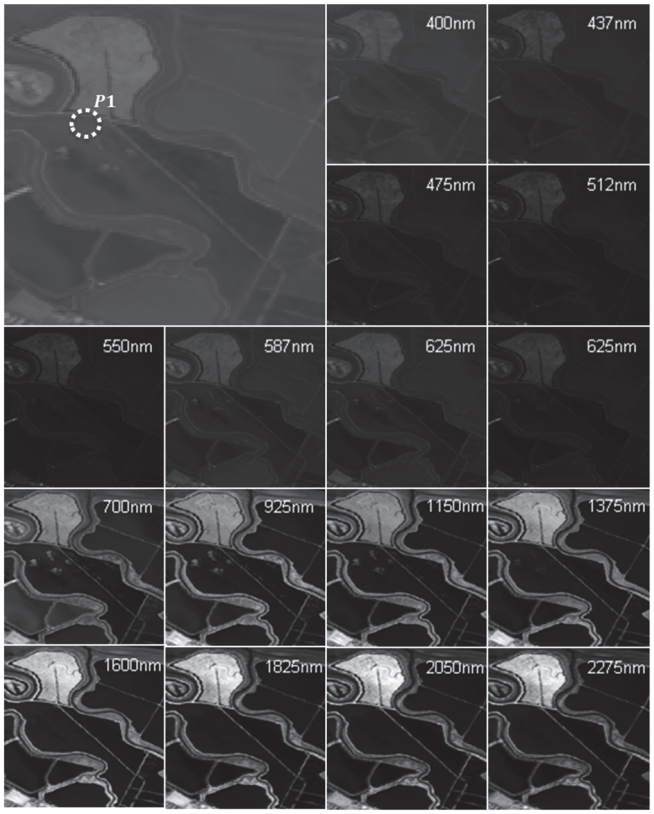

Figure 7. Spectral bands of "Moffet field" data cube with wavelengths ranging from 400 nm to 2275 nm. Each spectral slice has a spatial resolution of 128x128 pixels (Database 1).
Source: The authors.

The following section is divided into two subsections: in the first, the goal is to compare the sparsity of the spectral images when their visible and IR spectral band sets are separately and jointly sparsified. In the second, the analysis pretends to determine the performance of the proposed system in contrast with the parallelized CASSI systems.

5.1. Power analysis of the sparse representations

The objective of this experiment is to understand if the infrared extra content provides valuable information that increases sparsity in the images when the whole data cube $\mathbf{f}$ is represented by the sparsifying basis $\mathbf{\Psi}_{3D}$. The energy contained in the jointly transformed $\boldsymbol{\theta} = \mathbf{\Psi}_{3D}{}^{-1}\mathbf{f}$ is compared with the sorted vector's energy in coefficients $\widehat{\boldsymbol{\theta}} = [\boldsymbol{\theta}_V; \boldsymbol{\theta}_{IR}]$, where $\boldsymbol{\theta}_V = \mathbf{\Psi}_{3D}{}^{-1}\mathbf{f}_V$ and $\boldsymbol{\theta}_{IR} = \mathbf{\Psi}_{3D}{}^{-1}\mathbf{f}_{IR}$ are transformed separately.

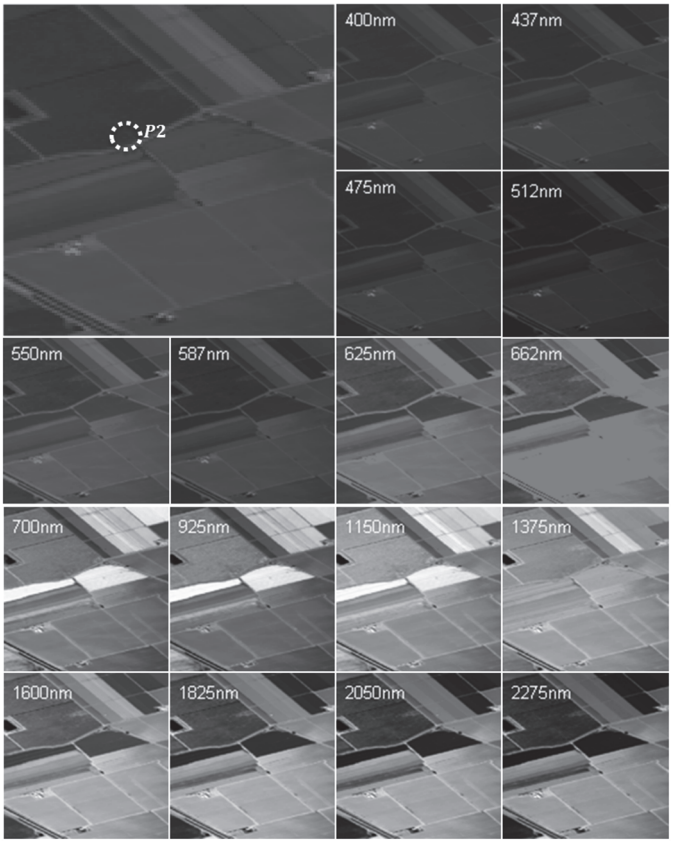

Figure 8. Spectral bands of "Salinas" data cube with wavelengths ranging from 400 nm to 2275 nm. Each spectral slice has a spatial resolution of 128x128 pixels (Database 2).
Source: The authors.

In order to do this, we compare the percentage of energy content as a function of the number of coefficients for $\boldsymbol{\theta}$ and $\widehat{\boldsymbol{\theta}}$. A zoomed version for the first 25 coefficients is shown in Fig. 9. It can be noticed that in Database 2 (Fig. 9 right) $\boldsymbol{\theta}$ has a sharper growth rate since more than 80% of the energy is contained in the first 5 coefficients compared with 60% achieved in the separated approach. Conversely, in the first Database (Fig. 9 left), $\boldsymbol{\theta}$ is less sparse compared with $\widehat{\boldsymbol{\theta}}$ since it has a slower power growth. It is important to take into account that regardless of the approach used to obtain the sparse representation, the total energy of each database must add up to the same value for both cases. The difference lies in the energy distribution among the coefficients.

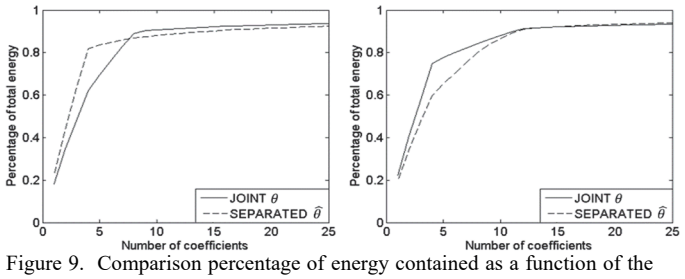

Figure 9. Comparison percentage of energy contained as a function of the number of coefficients for (a) Moffet field and (b) Salinas databases.
Source: The authors.

Under the assumption that the sparsity of the signal is highly related to the correlation between all the bands, a correlation analysis was undertaken, and the resulting 16x16 matrices are presented in Fig. 10. It can be observed that, as expected, Database 2 (right) presents a high correlation between all the visible bands. These, in turn, highly correlate with the latest infrared bands. Thus, the more correlated the bands of the data cube are, the greater the sparsity that is achieved.

5.2. Reconstruction *of the spectral images*

Diverse simulations were performed in order to determine the best Peak-Signal-to-Noise-Ratio (PSNR) of the reconstructed data cubes as a function of the transmittance, the compression ratio and the Gaussian noise applied to the measurements. In this section, the performance of the proposed DA-CASSI system and the conventional CASSI are compared by reconstructing of both databases.

To compare the performance of the DA-CASSI model with the traditional CASSI model, two different analyses were proposed. The first experiment focuses on the impact of two important factors, the coded aperture transmittance ξ and the number of snapshots taken (as a function of ρ); the second refers to the noise analysis for the best results obtained in the first part. For both analyses, the regularization parameter τ has been carefully selected so that optimum results are obtained; each experiment was repeated five times for every case, and the results were averaged. Finally, all simulations were conducted and timed using an Intel Core i7 3960x3.3 GHz processor with a 32 GB RAM memory.

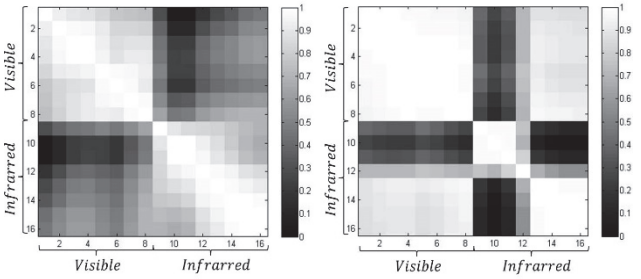

Figure 10. Correlation matrix for (a) Moffet field and (b) Salinas databases.
Source: The authors.

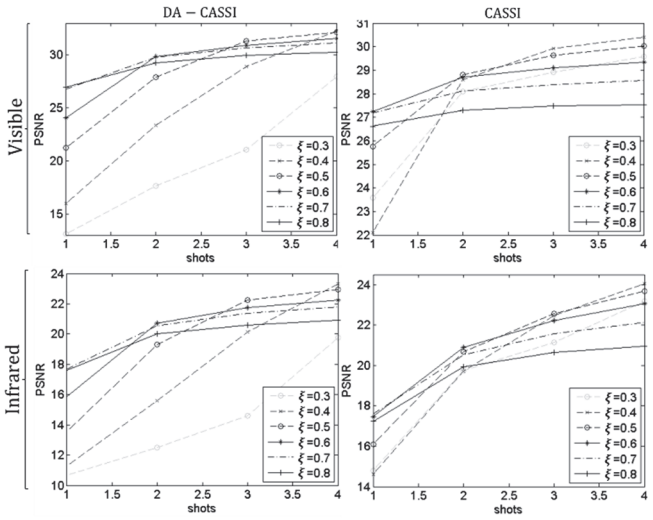

(a) Database 2. (Top-left) Visible using DA-CASSI, (Top-right) IR using DA-CASSI, (Bottom-left) visible using CASSI (Bottom-right) IR using CASSI.

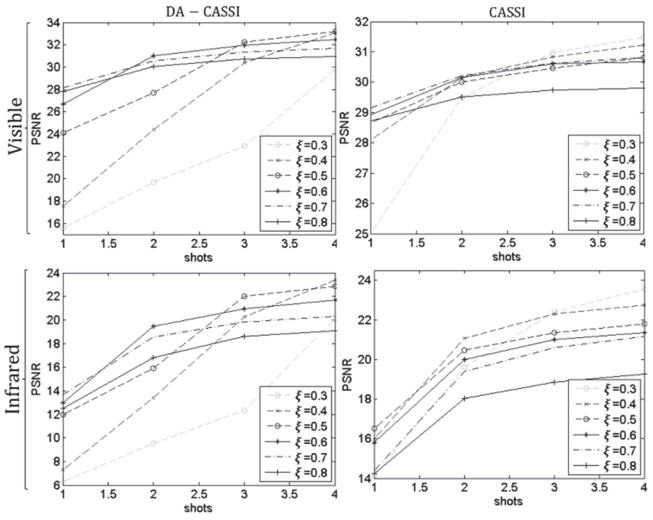

(b) Database 2. (Top-left) Visible using DA-CASSI, (Top-right) IR using DA-CASSI, (Bottom-left) Visible using CASSI (Bottom-right) IR using CASSI.

Figure 11. Impact of the transmittance ξ in the PSNR of the reconstructed images as a function of the number of snapshots *K* for (a) Moffet field and (b) Salinas data cubes.
Source: The authors

5.2.1. Optimal parameters analysis

In order to analyze the effect of the transmittance, we used several values of $\xi \in \{0.3, 0.4, 0.5, 0.6, 0.7, 0.8\}$. Transmittances above 0.8 are not analyzed given that they need to be solved by an extremely ill-posed inverse problem. Additionally, transmittances below 0.3 are also discarded due to their extremely low light efficiency [12]. In order to analyze the effect of the number of snapshots, we either varied *K* from 1 to 4 or we made the compression ratio $\rho = 13.18, 26.37, 39.55$ and 52.73%.

Fig. 11 manifests the reconstruction results obtained in the transmittance analysis at a different number of snapshots for both databases using the traditional CASSI and the proposed DA-CASSI. It can be observed that for a given ξ, and regardless of the database used, the reconstructed PSNR values increase as *K* increases. In addition, it can be noticed that, on average, the best results were always obtained for transmittances between 0.4 and 0.7.

A more detailed comparison can be quantitatively undertaken by analyzing Table 1, in which the averaged PSNR of the reconstructed data cubes are presented as a function of the optimal transmittance value for each number of shots.

From Table 1, it can be observed that: (i) as the two databases are the same size, the compression ratio ρ is the same for a given K, and in turn, its optimal transmittance value ξopt is inversely related to the number of shots; (ii) for

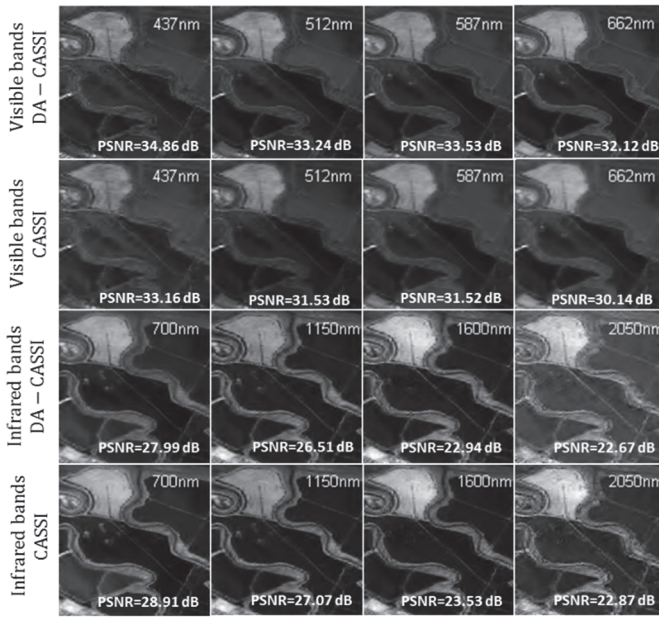

(a) Database 1. Four reconstructed bands from (first row) visible range using DA-CASSI (second row); visible range using CASSI (third row); IR range using DA-CASSI (last row) and IR range using CASSI.

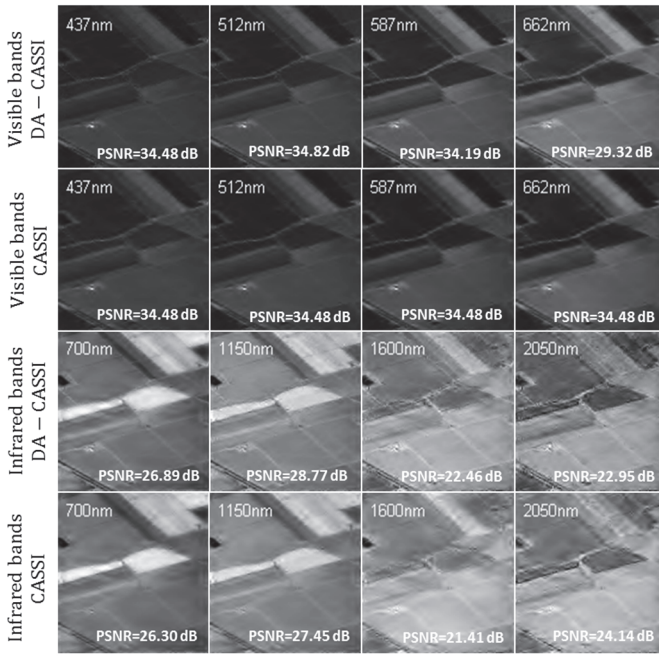

(b) Database 2. Four reconstructed bands from (first row) visible range using DA-CASSI (second row); visible range using CASSI (third row); IR range using DA-CASSI (last row) and IR range using CASSI.

Figure 12. Comparison of the best achieved reconstructed images (ξ=0.4 and ρ=52.73%) between CASSI and DA-CASSI for (a) Moffet field and (b) Salinas databases.
Source: The authors.

the visible range, the proposed DA- CASSI model recovers the bands with higher accuracy, yielding to a gain of up to 2 dB when more than 2 FPA shots are used; (iii) as a consequence of the low correlation between the infrared bands, the results obtained for this range are lower than in the visible range. However, for Database 2, due to the better sparsity boosted by the high correlation presented between the visible and the last four infrared bands, the proposed system is able to surpass the traditional CASSI by up to 1 dB when more than 2 snapshots are used. For both databases, the best results are obtained for ξ=0.4 and ρ=52.73%; the reconstructed bands with their corresponding attained PSNR are shown in Fig. 12. In summary, it is possible to asseverate that the improvement achieved in the DA-CASSI, is caused not only by the greater number of measurements used in the reconstruction per iteration compared with the CASSI system, but also by the correlation between the visible and infrared bands that boost the sparsity when this is high. Otherwise, the incoherence does not affect the performance as the sensing and sparsifying basis are the same for both models.

Table 1.
Averaged PSNR of the reconstructed bands for the optimal transmittance values as a function of *K*

Database	*K*	*ρ* (%)	ξ	DA-CASSI		CASSI	
			opt	**V [dB]**	**IR [dB]**	**V [dB]**	**IR [dB]**
No. 1	1	13,18	0.7	26,651	17,651	27,096	17,539
Moffet	2	26.37	0.6	29,839	20,739	28,725	20,941
128x128	3	39.55	0.5	30.297	21,362	29,660	22,442
x16	4	52.73	0.4	32,276	23,337	30,491	23.999
No. 2	1	13,18	0.7	28,092	13,581	29,178	14,447
Salinas	2	26.37	0.6	30.329	18,460	30,150	20,201
128x128	3	39.55	0.5	32,298	21,767	30,564	21,392
X16	4	52.73	0.4	33,221	23,629	31,215	22,814

Source: The authors.

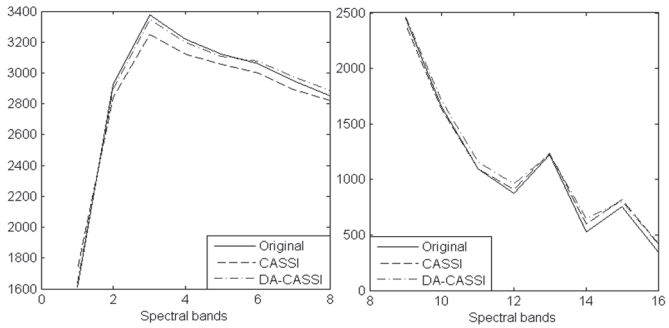

(a) Database 1. Reconstructed signatures of P1 in Fig. 9 for the: (left) Visible and (right) Infrared range.

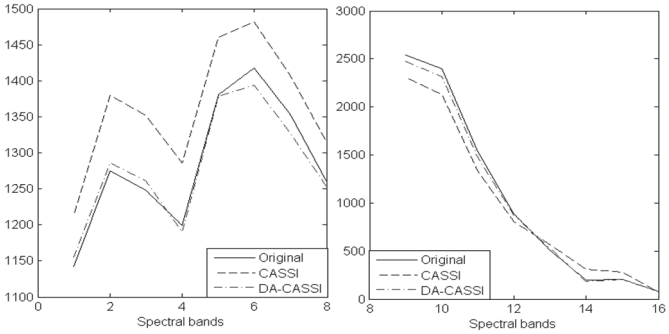

(b) Database 2. Reconstructed signatures of P1 in Fig. 9 for the: (left) Visible and (right) Infrared range.

Figure 13. Spectral signatures of P1 and P2 for ξ=0.4, ρ=52.73%. (a) Database 1. (b) Database 2. Source: The authors.

Table 2.
Averaged PSNR of the reconstructed bands for ξ=0.4 and ρ=52.73% as a function of the SNR noise.

Database	ρ(%)	SNR [dB]	DA-CASSI V [dB]	DA-CASSI IR [dB]	CASSI V [dB]	CASSI IR [dB]
No. 1 Moffet 128x128x16	52.73	10	28.931	17.591	29.008	20.832
		20	32.092	21.203	30.097	21.106
		30	32.204	21.556	30.321	21.423
		40	32.249	23.331	30.424	23.854
No. 2 Salinas 128x128x16	52.73	10	30.102	19.021	30.045	20.897
		20	33.064	22.989	30,984	22.331
		30	33.102	23.064	31.092	22.435
		40	33.145	23.399	31.213	22.528

Source: The authors.

In order to analyze the spectral performance, two spatial points were randomly chosen from each database (P1 and P2 in Fig. 7 and Fig. 8 respectively), and their spectral signatures are shown in Fig. 13. It can be observed that the signature reconstructed with the DA-CASSI fits better with the original curve.

5.2.2. Noise analysis

We have shown that the proposed system efficiently recovers the spectral images from just a few measurements, but in order to be truly powerful, it is necessary for the DA-CASSI system to be able to deal with noise. For this reason, the best performed measurements obtained in the analysis were corrupted with five different amounts of noise, and the results were then compared.

Table 2 shows the impact in the PSNR of the reconstructed images (with respect to the SNR) when adding noise to the measurements. As has been shown, the PSNR improves as the signal to noise ratio increases, ranging from 10 to 40 dB. It is worthwhile noting how the reconstruction quality increases as the noise decreases. It should also be noted that in most the cases, the DA-CASSI outperforms the traditional CASSI, even when there is noise present.

6. Conclusions

We have presented a variation of the CASSI system for spectral images in the visible and infrared range. The architecture design, as well as the mathematical model for the single-frame and multi-frame DA-CASSI system, have been proposed. The DA-CASSI system is a possible solution to reduce the implementation costs of such a broad spectrum acquisition system. The improvement achieved in the DA-CASSI is caused not only by the greater number of measurements used in the reconstruction compared with the CASSI system, but also by the correlation between the visible and infrared bands that boost the sparsity when this is high. In general, the PSNR of the reconstructed images with the proposed model reaches up to 33 dB and 23.32 dB for the visible and infrared bands, respectively.

References

[1] Arce, G.R., Brady, D.J., Carin, L., Arguello, H. and Kittle, D.S., Compressive coded aperture spectral imaging: an introduction. IEEE Signal Processing, 31(1), pp. 105-115, 2014. DOI: 10.1109/MSP.2013.2278763

[2] Gat, N., Imaging spectroscopy using tunable filters: A review, Proceedings of SPIE, pp. 50-64, 2000. DOI: 10.1117/12.381686

[3] Candès, E.J. and Wakin, M.B., An introduction to compressive sampling. IEEE Signal Processing Magazine, 25(2), pp. 21-30, 2008. DOI: 10.1109/MSP.2007.914731

[4] Ye, P., Arguello, H. and Arce, G.R., Spectral aperture code design for multi-shot compressive spectral imaging, In Digital Holography and Three-Dimensional Imaging (OSA), p. DWA6, 2010. DOI: 10.1364/DH.2010.DWA6

[5] Shaw, G.A. and Burke, H.H.K., Spectral imaging for remote sensing. Lincoln Laboratory Journal, [Online] 14(1), pp. 3-28, 2003. Available at: https://www.ll.mit.edu/publications/journal/journalarchives14-1.html#1

[6] Govender, M., Chetty, K. and Bulcock, H., A review of hyperspectral remote sensing and its application in vegetation and water resource studies. Water Sa, 33(2), 2007. DOI: 10.4314/wsa.v33i2.49049

[7] Gowen, A.A., O'Donnell, C., Cullen, P.J., Downey, G. and Frias, J.M., Hyperspectral imaging–an emerging process analytical tool for food quality and safety control. Trends in Food Science and Technology, 18(12), pp. 590-598, 2007. DOI: 10.1016/j.tifs.2007.06.001

[8] Cen, H. and He, Y., Theory and application of near infrared reflectance spectroscopy in determination of food quality. Trends in Food Science and Technology, 18(2), pp. 72-83, 2007. DOI: 10.1016/j.tifs.2006.09.003

[9] Ding, H.B. and Xu, R.J., Differentiation of beef and kangaroo meat by visible/near-infrared reflectance spectroscopy. Journal of Food Science, 64(5), pp. 814-817, 1999. DOI: 10.1111/j.1365-2621.1999.tb15918.x

[10] Duarte, M.F., and Baraniuk, R.G., Kronecker compressive sensing. IEEE Transactions on Image Processing, 21(2), pp. 494-504, 2012. DOI: 10.1109/TIP.2011.2165289

[11] Arguello, H. and Arce, G.R., Code aperture optimization for spectrally agile compressive imaging. Journal of the Optical Society of America, 28(11), pp. 2400-2413, 2011. DOI: 10.1364/JOSAA.28.002400

[12] Rueda, H., Arguello, H. and Arce, G.R., DMD-based implementation of patterned optical filter arrays for compressive spectral imaging. Journal of the Optical Society of America, 32(1), pp. 80-89, 2015. DOI: 10.1364/JOSAA.32.000080

[13] Kittle, D., Choi, K., Wagadarikar, A. and Brady, D.J., Multiframe image estimation for coded aperture snapshot spectral imagers. Applied Optics, 49(36), pp. 6824-6833, 2010. DOI: 10.1364/AO.49.006824

[14] Wu, Y., Mirza, I.O., Arce, G.R. and Prather, D.W., Development of a digital-micromirror-device-based multishot snapshot spectral imaging system. Optics Letters, 36(14), pp. 2692-2694, 2011. DOI: 10.1364/OL.36.002692

[15] Figueiredo, M., Nowak, R.D. and Wright, S.J., Gradient projection for sparse reconstruction: Application to compressed sensing and other inverse problems. IEEE Journal of Selected Topics in Signal Processing, 1(4), pp. 586-597, 2007. DOI: 10.1109/JSTSP.2007.910281

[16] Rueda, H., Calderon, A.R. and Arguello, H., Spectral selectivity in compressive spectral imaging based on grayscale coded apertures, Image Signal Processing and Artificial Vision (STSIVA), pp. 1-5, 2013. DOI: 10.1109/STSIVA.2013.6644929

[17] Green, R.O., Eastwood, M.L., Sarture, C.M., Chrien, T.G., Aronsson, M., Chippendale, B.J. and Williams, O., Imaging spectroscopy and the airborne visible/infrared imaging spectrometer (AVIRIS). Remote Sensing of Environment, 65(3), pp. 227-248, 1998. DOI: 10.1016/S0034-4257(98)00064-9

Y.P. Villa-Acuña, graduated with a BSc in Electronics Engineering in 2015 from the Universidad Industrial de Santander. Her research interests include digital signal processing, image processing and remote sensing.
ORCID: 0000-0001-7046-4984.

H. Arguello-Fuentes, graduated with a BSc in Electrical Engineering in 2000 and an MSc. in Electrical Power in 2003, both from the Universidad Industrial de Santander, Colombia. He was awarded his PhD in Electrical and Computer Engineering from the University of Delaware, United States. He is an associate professor in the Department of Systems Engineering at the Universidad Industrial de Santander, Colombia. His research interests include compressive sensing, high dimensional signal processing and computational imaging.
ORCID: 0000-0002-2202-253X.